Research Article | Vol. 24, No. 25 | 12 Dec 2016 | OPTICS EXPRESS 29269

Optics EXPRESS

High-speed spatial control of the intensity, phase and polarisation of vector beams using a digital micro-mirror device

KEVIN J. MITCHELL,[1] SERGEY TURTAEV,[2,3] MILES J. PADGETT,[1] TOMÁŠ ČIŽMÁR,[2] AND DAVID B. PHILLIPS[1,*]

[1] School of Physics and Astronomy, University of Glasgow, Glasgow G12 8QQ, Scotland, UK
[2] School of Science and Engineering, University of Dundee, Nethergate, Dundee DD1 4HN, Scotland, UK
[3] School of Life Sciences, University of Dundee, Nethergate, Dundee, DD1 4HN, Scotland, UK
[*] david.phillips@glasgow.ac.uk

Abstract: The dynamic spatial control of light fields is essential to a range of applications, from microscopy to optical micro-manipulation and communications. Here we describe the use of a single digital micro-mirror device (DMD) to generate and rapidly switch vector beams with spatially controllable intensity, phase and polarisation. We demonstrate local spatial control over linear, elliptical and circular polarisation, allowing the generation of radially and azimuthally polarised beams and Poincaré beams. All of these can be switched at rates of up to 4kHz (limited only by our DMD model), a rate ~2 orders of magnitude faster than the switching speeds of typical phase-only spatial light modulators. The polarisation state of the generated beams is characterised with spatially resolved Stokes measurements. We also describe detail of technical considerations when using a DMD, and quantify the mode capacity and efficiency of the beam generation. The high-speed switching capabilities of this method will be particularly useful for the control of light propagation through complex media such as multimode fibers, where rapid spatial modulation of intensity, phase and polarisation is required.

OCIS codes: (050.1380) Binary optics; (050.1970) Diffractive optics; (050.4865) Optical vortices.

References and links

1. X. Hao, C. Kuang, T. Wang, and X. Liu, "Effects of polarization on the de-excitation dark focal spot in STED microscopy," J. Opt. **12**, 115707 (2010).
2. V. Niziev and A. Nesterov, "Influence of beam polarization on laser cutting efficiency," J. Phys. D Appl. Phys. **32**, 1455 (1999).
3. S. Pereira and A. Van de Nes, "Superresolution by means of polarisation, phase and amplitude pupil masks," Opt. Commun. **234**, 119–124 (2004).
4. Q. Zhan, "Trapping metallic rayleigh particles with radial polarization," Opt. Express **12**, 3377–3382 (2004).
5. M. Friese, T. Nieminen, N. Heckenberg, and H. Rubinsztein-Dunlop, "Optical alignment and spinning of laser-trapped microscopic particles," Nature **394**, 348–350 (1998).
6. Z. Bouchal and R. Celechovskỳ, "Mixed vortex states of light as information carriers," New J. Phys. **6**, 131 (2004).
7. G. Milione, M. P. Lavery, H. Huang, Y. Ren, G. Xie, T. A. Nguyen, E. Karimi, L. Marrucci, D. A. Nolan, R. R. Alfano *et al.*, "4× 20 gbit/s mode division multiplexing over free space using vector modes and a q-plate mode (de) multiplexer," Opt. Lett. **40**, 1980–1983 (2015).
8. S. Popoff, G. Lerosey, R. Carminati, M. Fink, A. Boccara, and S. Gigan, "Measuring the transmission matrix in optics: an approach to the study and control of light propagation in disordered media," Phys. Rev. Lett. **104**, 100601 (2010).
9. S. Bianchi and R. Di Leonardo, "A multi-mode fiber probe for holographic micromanipulation and microscopy," Lab Chip **12**, 635–639 (2012).
10. T. Čižmár and K. Dholakia, "Exploiting multimode waveguides for pure fibre-based imaging," Nat. Commun. **3**, 1027 (2012).
11. J. Carpenter, B. J. Eggleton, and J. Schröder, "110x110 optical mode transfer matrix inversion," Opt. Express **22**, 96–101 (2014).
12. C. Maurer, A. Jesacher, S. Bernet, and M. Ritsch-Marte, "What spatial light modulators can do for optical microscopy," Laser Photon. Rev. **5**, 81–101 (2011).
13. J. A. Davis, D. M. Cottrell, J. Campos, M. J. Yzuel, and I. Moreno, "Encoding amplitude information onto phase-only filters," Appl. Opt. **38**, 5004–5013 (1999).

#275967 http://dx.doi.org/10.1364/OE.24.029269
Journal © 2016 Received 16 Sep 2016; revised 15 Oct 2016; accepted 16 Oct 2016; published 9 Dec 2016

Optics EXPRESS

14. R. Di Leonardo, F. Ianni, and G. Ruocco, "Computer generation of optimal holograms for optical trap arrays," Opt. Express **15**, 1913–1922 (2007).
15. R. W. Bowman, G. M. Gibson, A. Linnenberger, D. B. Phillips, J. A. Grieve, D. M. Carberry, S. Serati, M. J. Miles, and M. J. Padgett, "'red tweezers': Fast, customisable hologram generation for optical tweezers," Comput. Phys. Commun. **185**, 268–273 (2014).
16. C. Maurer, A. Jesacher, S. Fürhapter, S. Bernet, and M. Ritsch-Marte, "Tailoring of arbitrary optical vector beams," New J. Phys. **9**, 78 (2007).
17. X.-L. Wang, J. Ding, W.-J. Ni, C.-S. Guo, and H.-T. Wang, "Generation of arbitrary vector beams with a spatial light modulator and a common path interferometric arrangement," Opt. Lett **32**, 3549–3551 (2007).
18. G. S. Gordon, F. Feng, Q. Kang, Y. Jung, J. Sahu, and T. Wilkinson, "Coherent, focus-corrected imaging of optical fiber facets using a single-pixel detector," Opt. Lett. **39**, 6034–6037 (2014).
19. Y. Arita, M. Mazilu, T. Vettenburg, E. M. Write, and K. Dholakia, "Rotation of two trapped micro particles in vacuum: observation of optically mediated parametric resonances," Opt. Lett. **40**, 4751–4754 (2015).
20. L. Marrucci, C. Manzo, and D. Paparo, "Optical spin-to-orbital angular momentum conversion in inhomogeneous anisotropic media," Phys. Rev. Lett. **96**, 163905 (2006).
21. D. Naidoo, F. S. Roux, A. Dudley, I. Litvin, B. Piccirillo, L. Marrucci, and A. Forbes, "Controlled generation of higher-order Poincaré sphere beams from a laser," Nat. Photon. **10**, 327–332 (2016).
22. N. Radwell, R. Hawley, J. Götte, and S. Franke-Arnold, "Achromatic vector vortex beams from a glass cone," Nat. Commun. **7**, 10564 (2016).
23. D. B. Phillips, M.-J. Sun, J. M. Taylor, M. P. Edgar, S. M. Barnett, G. G. Gibson, and M. J. Padgett, "Adaptive foveated single-pixel imaging with dynamic super-sampling," arXiv preprint arXiv:1607.08236 (2016).
24. B. R. Brown and A. W. Lohmann, "Complex spatial filtering with binary masks," Appl. Opt. **5**, 967–969 (1966).
25. Y.-X. Ren, M. Li, K. Huang, J.-G. Wu, H.-F. Gao, Z.-Q. Wang, and Y.-M. Li, "Experimental generation of laguerre-gaussian beam using digital micromirror device," Appl. Opt. **49**, 1838–1844 (2010).
26. V. Lerner, D. Shwa, Y. Drori, and N. Katz, "Shaping laguerre–gaussian laser modes with binary gratings using a digital micromirror device," Opt. Lett. **37**, 4826–4828 (2012).
27. M. Mirhosseini, O. S. Magana-Loaiza, C. Chen, B. Rodenburg, M. Malik, and R. W. Boyd, "Rapid generation of light beams carrying orbital angular momentum," Opt. Express **21**, 30196–30203 (2013).
28. D. Stuart, O. Barter, and A. Kuhn, "Fast algorithms for generating binary holograms," arXiv preprint arXiv:1409.1841 (2014).
29. S. A. Goorden, J. Bertolotti, and A. P. Mosk, "Superpixel-based spatial amplitude and phase modulation using a digital micromirror device," Opt. Express **22**, 17999–18009 (2014).
30. D. B. Conkey, A. M. Caravaca-Aguirre, and R. Piestun, "High-speed scattering medium characterization with application to focusing light through turbid media," Opt. Express **20**, 1733–1740 (2012).
31. M. Plöschner, T. Tyc, and T. Čižmár, "Seeing through chaos in multimode fibres," Nat. Photon. **9**, 529–535 (2015).
32. D. Wang, E. H. Zhou, J. Brake, H. Ruan, M. Jang, and C. Yang, "Focusing through dynamic tissue with millisecond digital optical phase conjugation," Optica **2**, 728–735 (2015).
33. W.-H. Lee, "Binary computer-generated holograms," Appl. Opt. **18**, 3661–3669 (1979)
34. J. Courtial, "Self-imaging beams and the guoy effect," Opt. Commun. **151**, 1–4 (1998).
35. R. Dorn, S. Quabis, and G. Leuchs, "Sharper focus for a radially polarized light beam," Phys. Rev. Lett. **91**, 233901 (2003).
36. L. Allen, M. W. Beijersbergen, R. Spreeuw, and J. Woerdman, "Orbital angular momentum of light and the transformation of laguerre-gaussian laser modes," Phys. Rev. A **45**, 8185 (1992).
37. E. Galvez, P. Crawford, H. Sztul, M. Pysher, P. Haglin, and R. Williams, "Geometric phase associated with mode transformations of optical beams bearing orbital angular momentum," Phys. Rev. Lett. **90**, 203901 (2003).
38. J. Dyment, "Hermite-gaussian mode patterns in GaAs junction lasers," Appl. Phys. Lett. **10**, 84–86 (1967).
39. T. Čižmár, M. Mazilu, and K. Dholakia, "In situ wavefront correction and its application to micromanipulation," Nat. Photon. **4**, 388–394 (2010).
40. A. M. Beckley, T. G. Brown, and M. A. Alonso, "Full Poincaré beams," Opt. Express **18**, 10777–10785 (2010).
41. E. J. Galvez, S. Khadka, W. H. Schubert, and S. Nomoto, "Poincaré-beam patterns produced by nonseparable superpositions of laguerre–gauss and polarization modes of light," Appl. Opt. **51**, 2925–2934 (2012).
42. M. P. Edgar, G. M. Gibson, R. W. Bowman, B. Sun, N. Radwell, K. J. Mitchell, S. S. Welsh, and M. J. Padgett, "Simultaneous real-time visible and infrared video with single-pixel detectors," Sci. Rep. **5**, 10669 (2015).
43. L. Gong, Y. Ren, W. Liu, M. Wang, M. Zhong, Z. Wang, and Y. Li, "Generation of cylindrically polarized vector vortex beams with digital micromirror device," J. Appl. Phys. **116**, 183105 (2014).
44. R. Liu, F. Li, M. Padgett, and D. Phillips, "Generalized photon sieves: fine control of complex fields with simple pinhole arrays," Optica **2**, 1028–1036 (2015).
45. S. Popoff, G. Lerosey, M. Fink, A. C. Boccara, and S. Gigan, "Image transmission through an opaque material," Nat. Commun. **1**, 81 (2010).

Optics EXPRESS

1. Introduction

Spatial control over the transverse polarisation of light beams, in addition to the shaping of their intensity and phase, is useful in a variety of applications ranging from microscopy to optical micro-manipulation and communications. In particular, shaping of the transverse polarisation also yields control over the axial polarisation structure in tightly focused beams. For example, in stimulated emission-depletion (STED) super-resolution microscopy, an azimuthally polarised depletion beam improves the resolution by minimising its on-axis electric field [1]. Conversely, a tightly focused radially polarised beam maximises the on-axis electric field leading to a sharper focus which has further applications in micro-machining and microscopy [2, 3]. In optical trapping, a radially polarised beam potentially improves the trapping efficiency of metallic nano-particles [4], and a circular polarisation state exerts torque on birefringent particles making them spin in a direction controlled by the handedness of the incoming beam [5]. In optical communications the polarisation state and the spatial mode provide degrees of freedom for the encoding of information [6, 7]. In addition to the generation of beams with a desired spatially-varying polarisation, their rapid modulation is also a highly beneficial capability. In particular the fast switching of beams with spatially varying and arbitrarily controllable intensity, phase and polarisation can be used to speed up the measurement of the transmission characteristics of turbid media, helping to transform complex multiple scattering environments into precise optical components [8, 9]. In addition to phase modulation, the manipulation of polarisation is essential to fully control the propagation of light through multiply scattering environments [10, 11].

Phase-only liquid crystal based spatial light modulators (LC-SLMs) are widely used to generate arbitrarily structured beams in many of the applications described above [12]. A variety of phase patterning techniques have been reported for the structuring of both the 2D phase and intensity (albeit with reduced efficiency) of light beams [13–15]. Such techniques have also been extended to use LC-SLMs to generate vector beams with arbitrary transverse polarisation structures [16–19]. However, LC-SLM based techniques are typically limited by a switching rate on the order of ~100 Hz due to the viscosity of the liquid crystal. There are also a range of other methods to create specific (but not completely arbitrary) intensity, phase and polarisation patterns. For example Q-plates act like half wave plates which have spatially varying orientations of their optical axes [20, 21], and glass cones can produce radially or azimuthally polarised beams by exploiting the spatial and polarisation dependent phase shifts imparted by light undergoing total internal reflection [22].

For arbitrary control of beam structure, an alternative beam shaping technology to that of LC-SLMs is the digital micro-mirror device (DMD). Whereas the LC-SLMs enable pixel-by-pixel control of optical phase, DMDs enable pixel-by-pixel binary (on/off) control of intensity. A major advantage of DMDs over LC-SLMs is their enhanced switching rate, with some models capable of switching at rates in excess of 20kHz [23]. In addition to conventional intensity masking, a binary amplitude mask can also diffractively shape both the phase and intensity of an incident beam [24]. However, this diffractive mode of operation generally implies a reduction of efficiency compared to LC-SLMs. This trade-off between modulation speed and efficiency has been recently exploited to generate rapidly switchable arbitrarily structured scalar beams using DMDs [25–30]. In this work we adopt a similar approach and demonstrate the use of a DMD for the generation and high-speed switching of arbitrary vector beams, i.e. beams for which we have local spatial control over the intensity, phase and polarisation. We describe technical considerations of using a DMD, measure the output polarisation states using spatially resolved Stokes measurements, and quantify the efficiency of the beam generation.

Optics EXPRESS

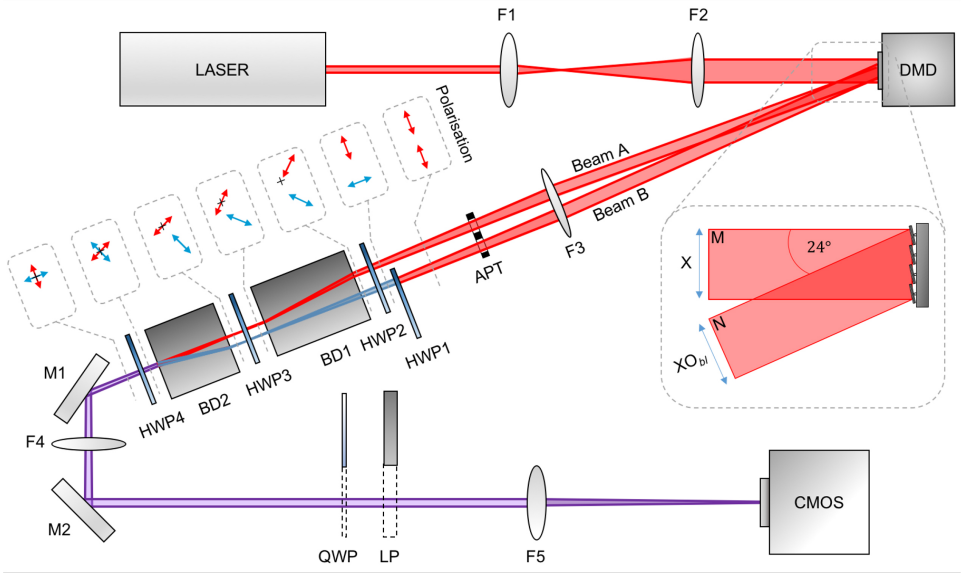

Fig. 1. **Experimental set-up**: The laser beam is generated by a Zeeman stabilised HeNe laser (*Neoark corp* Neo-262). The focal length of lens F1 = 40 mm, and F2 = 160 mm. The DMD is a *Texas Instruments* DLP LightCrafter evaluation model with a 0.3 WVGA chipset. F3 = 300 mm, and APT is a bespoke aperture designed to pass only beams A and B whilst blocking all other orders diffracted from the DMD. HWP1-HWP4 are multi-order half-wave plates. BD1 (*ThorLabs* BD40) and BD2 (*ThorLabs* BD27) are calcite beam displacers. M1 and M2 are silvered mirrors. F4 = 200 mm, and F5 = 150 mm. QWP and LP are a quarter-wave plate and a linear polariser that can be inserted before the CMOS camera (we used a *Prosilica* GC660, or a high-speed *Mikrotron* EoSens CL MC1362) to measure the spatially resolved polarisation states of the generated beams. The DMD patterns were designed using a *LabVIEW* program, and two different interface options were used: patterns were either uploaded directly to the DMD via the mini HDMI link for 60 Hz real-time control, or saved as 1-bit bitmaps and preloaded onto the DMD internal memory via USB link, to be played back in high-speed at up to 4 kHz. The inset shows the angles of incident and reflected light on the DMD.

2. Experimental set-up

Figure 1 shows a schematic of the experimental set-up. It is based on the LC-SLM driven scheme described in the supplementary material of [31], which was previously used to measure the complex transmission matrix of a multimode fibre and generate a full basis of vector fibre modes (~500). For the present work this scheme was chosen as it offers a high level of stability, due to the common pathway taken by both beams through the optical system, which minimises the effects of drift in the relative path lengths. A horizontally linearly polarised Helium-Neon laser beam is expanded (using lenses F1 and F2) and collimated to overfill the active area of the DMD chip. It is helpful to ensure that the orientation of the linearly polarised light incident on the DMD is parallel or perpendicular to the axis of rotation of the micro-mirrors. This prevents undesired path length changes due to any differences in the polarisation dependent Fresnel coefficients of the mirrors introducing ellipticity into the beam polarisation after reflection from the DMD. The pattern displayed on the DMD is designed to diffract light into two independent orders, transmitted at different angles from the DMD, denoted here beams A and B. The DMD pattern also enables independent spatial control of the local intensity and phase of light diffracted into each order, more details of which are given below in Section 3. Lens F3 collects the transmitted

Optics EXPRESS

beams, and after this an aperture blocks unwanted diffracted orders. The polarisation of beam B is then rotated by 90° using half-wave plate HWP1. Two beam displacers (BD1 and BD2) are then used to overlap the beams which are now of orthogonal polarisations back onto a common axis. Half-wave plates HWP2 and HWP3 are used to rotate the polarisation of both beams A and B by a fixed amount. This enables control of the combined displacement of the beams with respect to one another as they pass through the beam displacers. HWP3 is used to rotate the polarisations of both overlapped beams so that they are once again either parallel or perpendicular to the tilt axis of mirrors M1 and M2. This means any difference in path length between the vertical and horizontally polarised components due to reflection from these mirrors can be accommodated in the DMD pattern design (more detail below in Sec. 3). The relative polarisations of beams A and B as they pass through the beam displacers is also shown in Fig. 1. Lenses F4 and F5 re-image the vector beam onto a CMOS camera. The quarter-wave plate (QWP) and linear polariser (LP) can be translated in and out of the beam and are used to make spatially resolved Stokes measurements, more details of which are given below in Sec. 4.

We now also note some technical details of the optical set-up, and some specific points related to the use of a DMD. During alignment, the overlap of the beams can be measured using the camera, and fine tuned by varying the period of the gratings in the DMD pattern, and the angles of the beam displacers. We note that for an arbitrarily oriented linear input polarisation, each beam displacer outputs two parallel but spatially separated beams of orthogonal linear polarisation. Therefore after two beam displacers there are four output beams. The alignment procedure is as follows: first the beam displacers are both rotated so that two of the outgoing beams are co-linear, at this point taking no account of the power sent into each of the four beams. Next HWP2 and HWP3 are rotated until the power in the collinear outgoing beams is maximised. The orientation of HWP2 and HWP3 is chosen so that the incoming polarisation of each beam is matched to the orientation of the beam displacer, resulting in a minimal loss of power in beams A and B as they are overlaid (as depicted in Fig. 1).

The aperture (APT) positioned before the beam displacers (near but not exactly at the Fourier plane of the DMD due to space constraints) is useful to remove other diffraction orders during the alignment process. However once alignment is complete, to minimise any undesired spatial filtering due to its placement in the wrong plane, we found that this aperture could be removed. A small modification to the set-up also enabled us to measure the quality of vortex beam generation in the image plane of the DMD. To do this we added an additional lens after lens F5 (of focal length 150 mm), and moved the camera to the back focal plane of the additional lens, which now places the camera in an image plane of the DMD. In this scheme we also placed an aperture centred on the vector beam at the back focal plane of lens F5 which acted as a spatial filter to remove any other undesired diffraction orders.

The angle at which the incident beam strikes the DMD face is also important. The micro-mirrors tilt about their own axes by +/-12° to occupy their on/off states, which leads to transmitted light (including the undiffracted zero order beam) undergoing much larger angular deviations than in the case of reflection-mode LC-SLMs (where the undiffracted zero-order simply undergoes a reflection from the plane parallel to the SLM chip). The case for DMDs is shown in the expanded schematic of the DMD inset in Fig. 1: if light is incident normal to the DMD face (from direction M in the schematic in Fig. 1), undiffracted light will nominally be transmitted at an angle of 24° in direction N (rather than back towards the source at 0° as in the case for reflection-mode LC-SLMs). As shown in the inset, this leads to a lateral compression of the field in the x-direction by an obliquity factor $O_{bl} \approx \cos(24) \approx 0.91$. A compression in one dimension only can lead to aberrations in the output field, and so this factor can be corrected for in the pattern by laterally pre-stretching by a factor of $1/O_{bl}$. Other incident angles result in other correction obliquity factors, and in general $O_{bl}(\theta) \approx \cos(\theta + 24)$, where θ is the angle of incidence of light striking the DMD (measured from the chip normal in degrees). Therefore an incident angle of -24° (i.e.

Optics EXPRESS

from direction N) is preferred as this results in transmission normal to the DMD face in direction M, with an obliquity factor of unity and therefore no correction is necessary [32].

The obliquity factor here is described approximately as in reality it also depends upon the diffraction angle of the order. There is also an additional effect which causes a further small angular deviation of the transmitted beam: as each mirror rotates about its own axis, light reflecting off each mirror travels a different path length, and so a wavelength dependent phase step is imparted to the transmitted light beam, from one mirror to the next. This results in an additional phase tilt across the transmitted beam, which once again slightly alters its transmission angle, and therefore also modifies the obliquity factor correction.

3. Binary amplitude hologram design

We now describe the design of the binary DMD transmittance hologram to encode arbitrary vector beams at the output of our optical system (i.e. at the camera plane in Fig. 1). It was shown in the 1960s that binary amplitude masks can be used to shape both the intensity and phase of light [24]. In particular, the computer-generated hologram method enables the design of a binary amplitude grating in which the first diffraction order will possess the desired spatial intensity and phase profile [33]. The pitch of the grating controls the angle of the first diffraction order. Spatially varying intensity and phase modulation is then achieved by locally varying the duty cycle of the grating (i.e. the local width of the apertures) to control the diffracted intensity, and locally varying the lateral phase of the grating (i.e. the local lateral position of the apertures) to control the optical phase of the diffracted light. Therefore the binary transmittance function $T(x, y)$ which encodes a target *scalar* complex field $\mathbb{S}(x, y) = S(x, y)e^{i\phi_S}$ that propagates along its first diffraction order is given by:

$$T(x, y) = \frac{1}{2} + \frac{1}{2}\text{sgn}[\cos(p(x, y)) + \cos(q(x, y))], \tag{1}$$

where:

$$p(x, y) = \phi_S(x, y) + \phi_{tilt}(x, y), \tag{2}$$

$$q(x, y) = \arcsin(S(x, y)/S_{max}). \tag{3}$$

Here x and y are Cartesian coordinates with their origin at the centre of the DMD, $\text{sgn}(x)$ is the sign function, $\phi_S(x, y)$ is the phase of the target scalar field, and $\phi_{tilt} = 2\pi(u_0 x + v_0 y)$ is a linear phase ramp which is used to specify the angle of the first order of diffraction, in which the target field will appear. u_0 and v_0 are constants determining the gradient of the phase ramp. $S(x, y)$ is the amplitude of the target scalar field, with maximum value S_{max}. $T(x, y)$ will also generate additional unwanted diffraction orders. In order to reduce the likelihood of the target beam overlapping with these other diffraction orders, the maximum spatial frequencies of the patterns $S(x, y)$ and $\phi_S(x, y)$ should not exceed $(u_0^2 + v_0^2)^{\frac{1}{2}}$. We note that Eqn. 1 produces the desired spatial mode in an image plane of the DMD provided that the additional unwanted orders are blocked in the Fourier plane of the DMD. In our experiment, all of the scalar components of our modes are propagation invariant (and therefore have the same profile in the image plane or Fourier plane save for a magnification and a phase term [34]) and so we can position the camera to view the generated beam in either the image plane or Fourier plane. In the general case, the target beam will be formed in the image plane of the DMD, and to obtain the target beam in the Fourier plane then $\mathbb{S}(x, y)$ must be defined by the Fourier transform of the target beam.

In our experiment we aim to create a target *vector* beam of arbitrary intensity, phase and polarisation ($\vec{E}(x, y)$) the general form of which is given by:

$$\vec{E}(x, y) = \begin{bmatrix} E_A(x, y)e^{i\phi_A} \\ E_B(x, y)e^{i\phi_B} \end{bmatrix}, \tag{4}$$

Optics EXPRESS

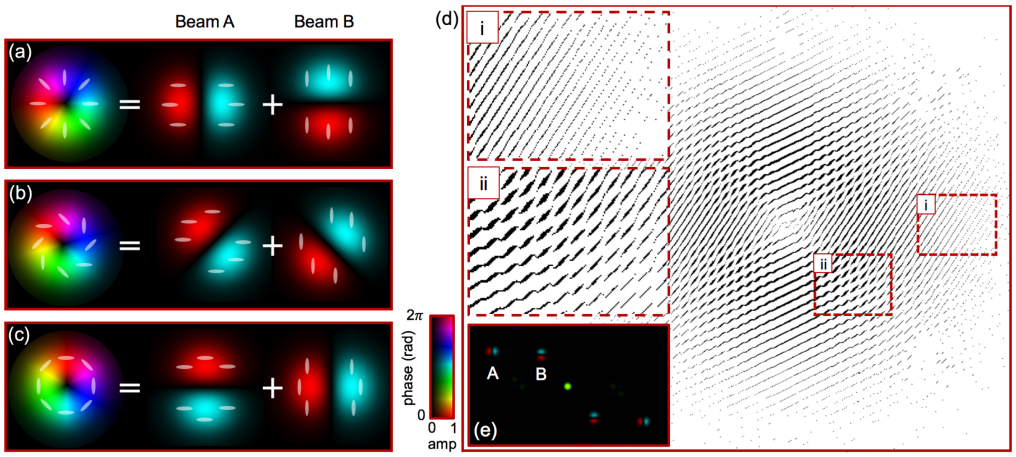

Fig. 2. **DMD hologram design**: (a) A radially polarised vector vortex beam with a Laguerre-Gaussian ($LG_{\ell=1,p=0}$) intensity profile can be formed from the addition of a horizontally polarised Hermite-Gaussian ($HG_{n=1,m=0}$) spatial mode, and a vertically polarised $HG_{0,1}$ spatial mode. Here ℓ and p are the LG vortex and radial spatial mode indices respectively, and n and m are the HG spatial mode indices. (b) A chirally polarised vector vortex beam (i.e. the polarisation structure is chiral in nature) is formed from the addition of two rotated HG beams of orthogonal linear polarisations. (c) An azimuthally polarised vector vortex beam is formed from the addition of a horizontally polarised $HG_{0,1}$ spatial mode and a vertically polarised $HG_{1,0}$ spatial mode. (d) A binary transmittance function displayed on the DMD to generate the radially polarised beam shown in (a). This was designed using Eqns. 1-5, where $\mathbb{A}$ and $\mathbb{B}$ are the appropriate HG modes shown in (a) each incorporating a different phase tilt to transmit them in different directions. Here we show the negative of the transmission function (i.e. white represents regions where incident light is blocked, and black where it is transmitted). The insets show regions of the pattern in more detail: (i) a region that diffracts light predominantly into beam A, (ii) a region that diffracts a similar intensity of light into beams A and B. (e) A simulation of the field at the Fourier plane of the DMD when displaying the binary transmittance function shown in (d), showing beams A and B spatially separated and with independent intensity and phase profiles. The central beam is the zero diffraction order, and the beams are copied in the lower right quadrant due to the binary nature of the diffraction grating.

where $E_A(x,y)e^{i\phi_A}$ and $E_B(x,y)e^{i\phi_B}$ are two *scalar* fields of orthogonal linear polarisation and independently spatially controllable intensity (e.g. E_A^2 for field A) and phase (e.g. ϕ_A for field A). We therefore require a binary transmittance function which generates these two scalar beams diffracting at different angles. We note that upon transmission from the DMD these beams are both initially horizontally linearly polarised as described above, and one beam then undergoes a 90° rotation of its linear polarisation rendering them orthogonally polarised before they are overlaid onto a common optical axis. Therefore in the general case the two independent scalar fields (of common polarisation) transmitted by the DMD are given by: $\mathbb{A}(x,y) = A(x,y)e^{i(\phi_A+\phi_{A,tilt})}$ and $\mathbb{B}(x,y) = B(x,y)e^{i(\phi_B+\phi_{B,tilt})}$, where $\phi_{A,tilt}$ and $\phi_{B,tilt}$ are the phase ramps which specify the direction of each diffraction order. $T(x,y)$ is then calculated from a dual beam field given by the weighted complex interferometric sum of $\mathbb{A}$ and $\mathbb{B}$:

$$\mathbb{S}_{dual} = S_{dual}(x,y)e^{i\phi_{S,dual}(x,y)} = W_{rel}e^{i\phi_{global}}\mathbb{A} + (1 - W_{rel})\mathbb{B}, \tag{5}$$

where W_{rel} is a real number between 0 and 1 which specifies the relative power sent into beams A and B (for example the power is nominally the same when W_{rel} is set to 0.5). ϕ_{global} controls the relative global phase between the two orders. Therefore to design the dual beam

Optics EXPRESS

binary transmittance function using Eqn. 1, we now have $p(x, y) = \phi_{S,dual}(x, y)$ and $q(x, y) = \arcsin(S_{dual}(x, y)/S_{dual,max})$.

The functions $\mathbb{A}$ and $\mathbb{B}$ depend upon the target vector beam, and can be calculated by decomposing it into two orthogonal linearly polarised components. This process is similar to that described in [16] for the generation of vector beams using an LC-SLM. In general, the local polarisation state may be defined by a polarisation ellipse, and the relative local phase difference of the electric field of the two orthogonal linearly polarised components determines the ellipticity of the local polarisation state of the vector beam. For example a phase difference of zero (or π or 2π) radians specifies a linear polarisation state, a phase difference of $\pi/2$ radians specifies circular polarisation, and other phase values specify elliptical polarisation. The orientation of the major axis of the polarisation ellipse is specified by both the local relative phase and the local relative amplitude of the two orthogonal linearly polarised components. Therefore the intensity, phase and polarisation of the vector beams are necessarily coupled. However, similar to [16], our method enables full control of both phase and polarisation as we have arbitrary control of both (i) the relative phase of the electric field of each polarisation, and (ii) the relative phase of the oscillating electric field of adjacent spatial locations within the beam.

Figure 2 shows an example of the binary transmittance function calculated to generate a radially polarised vector beam [35]. As can be seen in Fig. 2(a), the vector beam has a helical *Pancharatnam-Berry* phase, indicating that the beam carries orbital angular momentum with a vortex charge of $\ell = 1$ [36]. This is a geometric phase arising from the rotation of the local polarisation state as the beam axis is orbited [20, 37]. The radially polarised beam can be decomposed into two orthogonal linearly polarised beams, each consisting of two lobes that are out of phase by π (and depending on the exact radial intensity profiles these orthogonally polarised beams may be described by Hermite-Gaussian HG_{10} and HG_{01} spatial modes [38].) The intensity and phase of these two fields therefore define functions $\mathbb{A}$ and $\mathbb{B}$ used to design the DMD pattern. In addition, $\mathbb{A}$ and $\mathbb{B}$ can also incorporate aberration correction phase functions if necessary. These functions are the phase conjugate of any phase distortions imparted to the beam anywhere along either of the two beam paths. If necessary these functions can be measured in-situ along each beam path independently using the methods described in [39]. We found that the phase flatness of our DMD model (described in the caption of Fig. 1) was extremely good and so this was unnecessary in our experiment.

Finally, the relative amplitude (W_{rel}) and global phase (ϕ_{global}) terms enable a simple way of empirically fine-tuning the hologram pattern to ensure accurate generation of the required polarisation states. W_{rel} is used to cancel any differences in diffraction efficiency with diffraction angle from the DMD (due to the envelope function of the diffraction grating). ϕ_{global} is used to accommodate any path length differences taken by beams A and B through the set-up.

4. Results

Vector beam generation and measurement: We first demonstrate the generation of uniformly polarised beams which combine light from both beam A and beam B with a controlled phase offset, and investigate their propagation stability by measuring the polarisation state in both the Fourier plane of the DMD (camera positioned as shown in Fig. 1) and image plane of the DMD (camera positioned after an additional lens as described in Sec. 2). The polarisation state across the beams was measured by performing spatially resolved Stokes measurements. This was achieved by measuring the intensity of light that was transmitted through the following six polariser configurations: vertical (a measure of $|E_v|^2$, where E_v is the vertical component of the electric field), horizontal ($|E_h|^2$), diagonal ($|E_d|^2$), anti-diagonal ($|E_a|^2$), left-handed circular ($|E_-|^2$), and right-handed circular ($|E_+|^2$). The final two measurements were achieved with the combination of a quarter-wave plate followed by a linear polariser as shown in Fig. 1). To transform these measurements into polarisation ellipses we follow the analysis detailed in [22] to

Optics EXPRESS

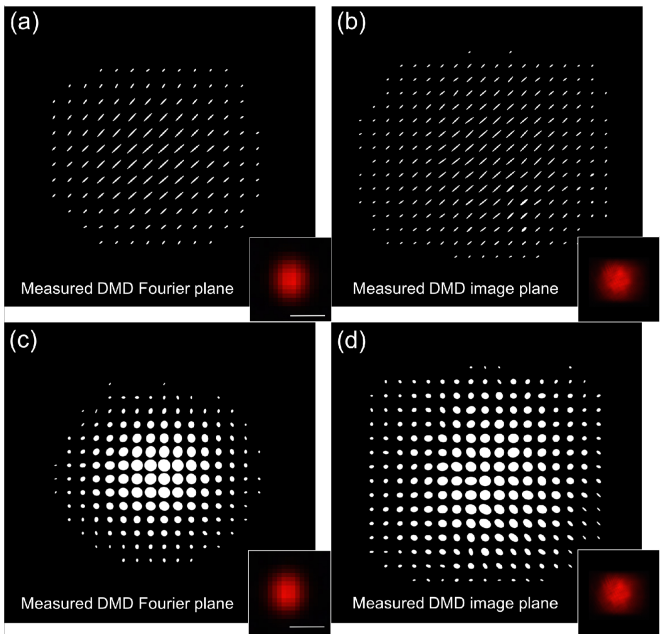

Fig. 3. **Experimentally generated vector beams with uniform polarisation**. Upper row: (a) Generation of a diffraction limited beam (i.e. generated by diffracting light from over the entire face of the DMD) of diagonal linear polarisation in the Fourier plane of the DMD. This is formed from beams A and B of equal power with a zero radian phase shift between their electric fields. Inset shows the intensity of the beam. Scale bar = 50μm. (b) The same beam as in (a) now viewed in the image plane of the DMD. (c) Generation of a diffraction limited beam of circular polarisation in the Fourier plane of the DMD. This is formed from beams A and B of equal power with a $\pi/2$ rad. phase shift between their electric fields. (d) The same beam as (c) now viewed in the image plane of the DMD.

calculate the magnitudes of the major (P_{major}) and minor (P_{minor}) ellipse axes, the orientation of the major axis (θ) and the handedness (h). Therefore:

$$P_{major} = \left[\frac{1}{2}(I_p + |L|)\right]^{\frac{1}{2}}, \quad P_{minor} = \left[\frac{1}{2}(I_p - |L|)\right]^{\frac{1}{2}}, \quad \theta = \frac{1}{2}\arg(L), \quad h = \mathrm{sgn}(V), \quad (6)$$

where:

$$I_p = \left[\left(|E_v|^2 - |E_h|^2\right)^2 + \left(|E_a|^2 - |E_d|^2\right)^2 + \left(|E_-|^2 - |E_+|^2\right)^2\right]^{\frac{1}{2}}, \quad (7)$$

$$L = \left(|E_v|^2 - |E_h|^2\right)^2 + i\left(|E_a|^2 - |E_d|^2\right)^2. \quad (8)$$

In all of our results the relative length of the major axis has been scaled in proportion to the local intensity of light in that region of the beam.

Figure 3 demonstrates the generation of vector beams with diagonal linear polarisation, and circular polarisation when utilising the full aperture of the DMD. Therefore a diffraction limited spot is created in the Fourier plane (Fig. 3(a) and 3c)). The measurements in the image plane of the DMD (Fig. 3(b) and 3(d)) reveal the Gaussian illumination intensity clipped by the rectangular aperture of the DMD. The key point here is that we see that the target polarisation is produced in both the Fourier and image plane of the DMD.

Next we investigate the generation of beams with spatially varying polarisation structures, as shown in Fig. 4. Figures 4(a)-4(c) show a comparison of numerically simulated and experimentally measured radially polarised beams, viewed both in the Fourier plane and the image plane

Optics EXPRESS

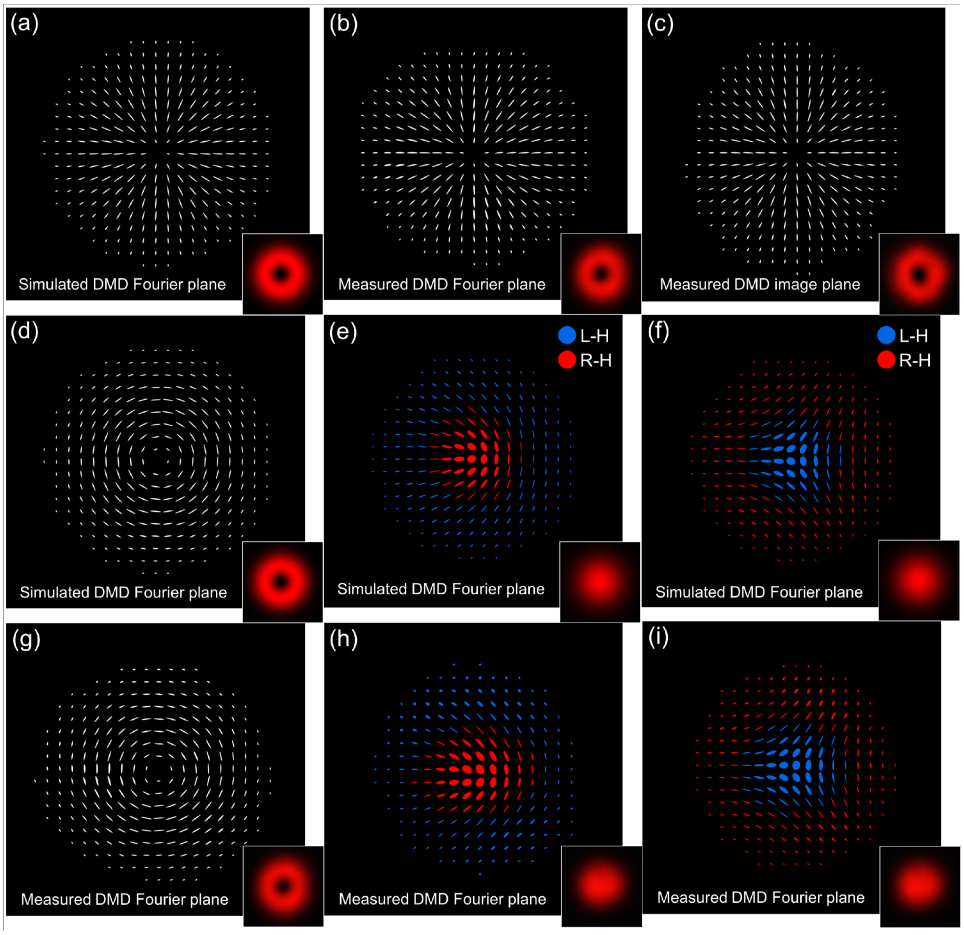

Fig. 4. **Comparison of simulated and experimentally generated vector beams with spatially varying polarisation**. Upper row: (a-c) A simulated (a) and experimentally measured (b,c) radially polarised vector vortex beam. (b) is measured in the Fourier plane of the DMD, while (c) is measured in the image plane of the DMD. Insets show the simulated/measured intensity of the field in each case. Middle row: (d-f) Simulated azimuthally polarised (d), Poincaré 'lemon' (e), and Poincaré 'star' (f) beams. In (e) and (f) the colour signifies the handedness of the local polarisation state. Lower row: (g-i) Experimentally generated and measured polarisation maps of the same beams as the rows above.

of the DMD. The design of the binary transmittance function to generate this radially polarised beam is described in Fig. 2(a), and shown in Fig. 2(d).

Figures 4(d)-4(f) show simulations of other beams of spatially varying structure, namely an azimuthally polarised beam (Fig. 4(d)), a Poincaré 'lemon' (Fig. 4(e)), and a Poincaré 'star' (Fig. 4(f), so called as its polarisation map looks like a 3 pointed star). Poincaré beams contain all polarisations on the Poincaré sphere [40]. Figures 4(g)-4(i) show experimentally measured examples of each beam. The design of the binary transmittance function to generate this azimuthally polarised beam is described in Fig. 2(c). The Poincaré beams were designed as described in reference [41]: beams A and B consisted of superpositions of Laguerre-Gaussian beams ($LG_{\ell,p}$). In the case of the Poincaré 'lemon', beam A is formed from the sum of $LG_{1,0}$+$LG_{0,0}$, while beam B is formed from $LG_{1,0}e^{i\pi}$+$LG_{0,0}$. In the case of the Poincaré 'star',

Optics EXPRESS

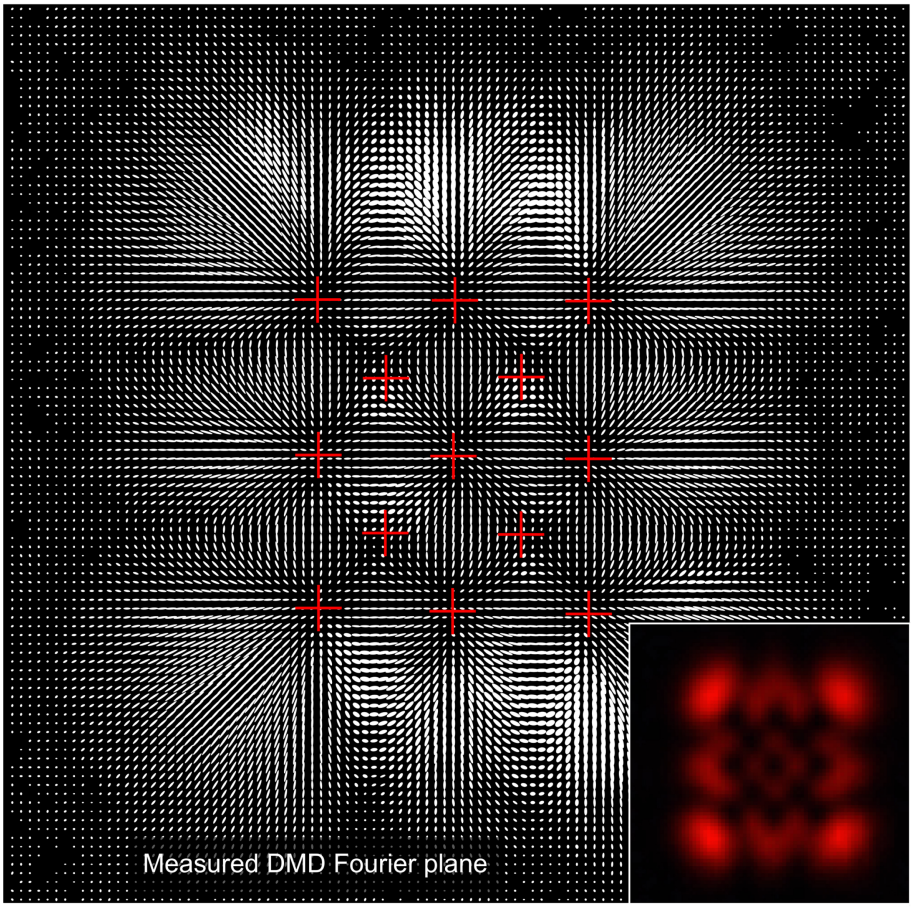

Fig. 5. **Higher order polarisation structuring**. Generation of a linearly polarised beam possessing a diagonal square lattice of polarisation vortices. The polarisation structure around each vortex alternates between a radial distribution and a 4-pointed star distribution. The expected position of each vortex is marked with a red cross. The inset shows the intensity pattern of the beam, where the vortices can clearly be seen. To create this structure beam A was formed from a $HG_{3,2}$ spatial mode, and beam B from a $HG_{2,3}$ spatial mode.

beam A is formed from the sum of $LG_{1,0}$+$LG_{0,0}$, while beam B is formed from $LG_{1,0}$+$LG_{0,0}e^{i\pi}$. In all cases we observe good agreement between our simulations and experiments. Finally, to demonstrate that our set-up is capable of creating higher order polarisation structures, Fig. 5 shows the experimental generation of a beam containing a more complex polarisation structure containing 13 polarisation vortices.

High-speed vector beam modulation: We now demonstrate the high speed switching capability of the DMD. Figure 6 shows a series of images of the beam once it had passed through a linear polariser, recorded with a high-speed camera (see caption of Fig. 1), as the pattern on the DMD is switched at a rate of 4kHz. We preloaded 10 patterns designed to switch the vector beam gradually from a radially polarised to azimuthally polarised state, by locally rotating the polarisation through a series of chirally polarised states. For each of the 10 preloaded patterns a full measurement of the polarisation state of the generated beams was made separately. Figure 6 shows these 10 polarisation maps adjacent to the high-speed camera images.

Optics EXPRESS

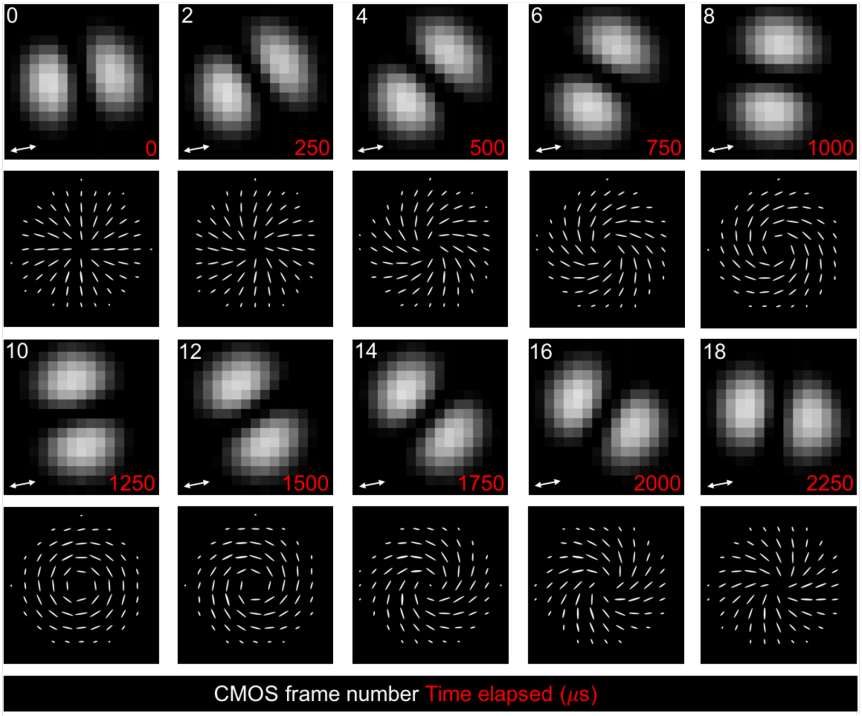

Fig. 6. **High-speed beam switching using a DMD** Upper panels (spinning lobe images): images of the generated beam captured through a static linear polariser at ~7 kHz with a high-speed camera, as the DMD cycles through a series of 10 pre-loaded patterns at a rate of 4 kHz. The orientation of the transmitted polarisation is shown as a white arrow in the lower left hand corner of each panel. We show every second camera frame, and the elapsed time of each frame is also shown in red. The high-speed rotation of the lobes indicates the rotation of the local polarisation within the beam from one DMD pattern to the next. Lower panels (polarisation maps): Experimentally reconstructed polarisation maps of the beam for each DMD pattern. The polarisation map data was not collected at high speed as it required the recording of multiple images of the beam transmitted through different polariser states as described in Section 4. Visualization 1 also shows the camera frames as a slow motion movie.

5. Discussion and conclusions

In this work we have demonstrated the use of a DMD for the generation of beams with spatially varying intensity, phase and polarisation. Our technique creates two beams of orthogonal polarisation which are then overlaid back onto the same optical axis with locally controllable relative intensity and phase. A key advantage of our set-up is its high stability, due to the common pathway taken by both beams through the optical system, which minimises the effects of drift in the relative path lengths. We have analysed the polarisation of the resulting beams using spatially resolved Stokes measurements, and show good agreement with theory. We have demonstrated a beam switching rate of up to 4 kHz, limited only by our DMD model (*Texas Instruments* DLP LightCrafter). This model of DMD also has the advantage of being relatively inexpensive (approximately an order of magnitude less than a typical LC-SLM), and so represents a low cost beam shaping device. More expensive and faster DMDs have switching rates in excess of 22 kHz [42] which is ~2 orders of magnitude higher than the fastest currently commercially available models of LC-SLM which operate at up to ~200 Hz. We also note that [43] demon-

Optics EXPRESS

strated the use of a DMD to generate cylindrically polarised vector vortex beams, although their set up did not enable arbitrary polarisation structuring.

We now discuss the theoretical number of independent vector spatial modes that can be generated with our set-up. As the same optical system can be used with an LC-SLM or a DMD we consider the spatial mode generation capacity of both devices here [31]. The number of independent spatial modes that can be produced by a spatial light modulator (DMD or LC-SLM) is related to the number of independently addressable pixels N possessed by the device. The width X (or height Y) of the addressable area in the focal plane of an SLM (for the purposes of this calculation here we assume a simplified system with a single Fourier transform lens) is defined by the pixel pitch p_x (or p_y), the wavelength λ and the focal length of the lens f. Therefore $X = (\lambda f)/(2p_x)$ and $Y = (\lambda f)/(2p_y)$, calculated from the maximum phase tilt that can be imparted to incident light by displaying the finest possible grating on the device, and applying the small angle approximation. Therefore, theoretically the maximum number of independent spatial modes that can be generated within the area XY by an LC-SLM is equal to the number of pixels on the device. For a typical LC-SLM with for example $N = 512 \times 512$ pixels, this suggests the possible generation of 262,144 modes. However in practice the usable number is often far lower as this estimate ignores the efficiency of the mode generation, and any coupling between pixels.

When using a DMD to create a target beam in the first diffraction order, the binary nature of the hologram always results in the generation of an accompanying conjugate field of equal power in the -1 diffraction order of the device, as can be seen in Fig. 2(e). This reduces the number of *independently* controllable spatial modes by approximately a factor of two compared to an LC-SLM possessing the same number of pixels (although in practice SLMs will also direct some light into their -1 diffraction orders, the level of which depends upon their phase bit depth). In addition, for both the LC-SLM and DMD cases there are also other considerations such as ensuring target modes are sufficiently separated from the zero and second orders of the diffraction pattern, and how large an area of zero intensity is required around each generated mode. To estimate the number of modes that can be usefully generated, it is instructive to estimate the number of (nominally) non-overlapping focussed spots that can be generated within a particular area in the Fourier plane of the DMD. The width d of a single diffraction limited spot can be estimated from the numerical aperture of the system: $d \sim 2\lambda f/D$, where D is the diameter of the Fourier transform lens. For example, in our experiment, if we restrict our region of interest for Beam A to 1/16 of the total addressable area in the Fourier plane (chosen as a quarter of the area of one quadrant), we find the number of spatial modes of a single polarisation, M_{scalar}, is given by: $M_{scalar} = (X^2)/(16d^2) = N/64$. This assumes that the DMD is square and so $X = Y$ and $p_x = p_y$ for simplicity. Therefore with the constraints set in this example, a DMD of resolution 512×512 pixels yields $M_{scalar} = 4096$ spatial modes. Using this example there is still ample room in the Fourier plane available to make use of a second equally sized region of interest in an adjacent quadrant where beam B can be diffracted to. Therefore the number of vector spatial modes (which also include the polarisation degree of freedom) is given by: $M_{vector} = 2M_{scalar} = 8192$. We note that in practice, any high spatial frequency phase aberrations present in the system may further limit the number of possible vector modes, as we require precise phase control between beam A and beam B. This being said, phase aberrations may be mitigated using in-situ wavefront correction which is capable of relatively high spatial frequency phase aberration correction [39]. Finally we note that DMDs have been successfully used in the past to generate large numbers of spatial modes [29].

The relatively high switching rates offered by DMDs are achieved at the expense of a reduction in diffractive beam shaping efficiency: the DMD essentially acts as a filter, the efficiency of which can be calculated from the overlap integral between the required complex field at the plane of the DMD (i.e. the target complex vector field back propagated through the optical system to the

Optics EXPRESS

plane of the DMD), and the actual field at the plane of the DMD [44]. Therefore assuming the DMD is illuminated by a plane wave, and that light rejected by OFF mirrors is simply blocked, the normalised *transmitted* efficiency E_{trans} (i.e. the fraction of transmitted light directed into the desired modes - beams A and B) is given by:

$$E_{trans} = \left| \frac{1}{N_E} \iint T(x,y)\mathbb{S}(x,y)^* \mathrm{dx\,dy} \right|^2, \tag{9}$$

$$N_E = \left[\iint |T(x,y)|^2 \mathrm{dx\,dy} \times \iint |\mathbb{S}(x,y)|^2 \mathrm{dx\,dy} \right]^{\frac{1}{2}}. \tag{10}$$

Here N_E is a normalisation factor, and in this case the limits of the integrals are set by the edges of the DMD display. The normalised *total* efficiency E_{total} (i.e. the fraction of light incident on the DMD that is transmitted into the desired modes) is then given by $E_{total} = fE_{trans}$, where f is the fraction of mirrors in the displayed DMD pattern that are turned ON. Equation 9 can also be used to calculate the theoretical efficiency of an LC-SLM, in this case by replacing the DMD transmittance function $T(x,y)$ with the field at the SLM, which is given by $e^{i\phi_{S,dual}(x,y)}$.

As can be seen from Eqn. 9, E_{total} is dependent upon the specific target vector beam. Furthermore, the efficiency of both LC-SLMs and DMDs is lowered when the patterns incorporate both phase and intensity modulation as is required here. Using Eqn. 9 we find the normalised total efficiency with which the DMD generates the beams shown here ranges from 2-5%, which is ~3-6% the efficiency of using an LC-SLM. However with the growing availability of relatively high power lasers and sensitive detectors, many applications are suited to the prioritisation of high switching speed over generation efficiency. For example, an active and fast growing area of research is in the characterisation of the transmission properties (i.e. the transmission matrix) of highly scattering media, such as glass diffusers, multimode fibers and biological material. This has the potential to transform such materials into exquisitely precise optical components through which images can be transmitted - offering new imaging opportunities in a variety of contexts. However the complexity of these media means that it requires a large number of polarisation resolved measurements (typically numbering at least in the thousands) to both characterise their light transmission properties, and also transmit spatially resolved image data through them [31,45]. Therefore in particular we anticipate that the fast generation of arbitrary vector beams will prove a useful technique to applications in this area.

Funding

EU FP7 Programme (FP7/2007-2013) REA grant agreement (608133); SUPA PaLS initiative; Royal Academy of Engineering; EPSRC (QuantIC, Grant no. EP/M01326X/1); ERC (TWISTS grant no. 192382).

Acknowledgments

We thank Neal Radwell for advice on the spatially resolved Stokes measurements, Johannes Courtial for making available his beam modelling software, and Graham Gibson for advice on the experimental set-up. ST acknowledges support from the EU FP7 Programme. MJP thanks the Royal Society and the Wolfson Foundation. TC acknowledges support from the SUPA PaLS initiative. DBP thanks the Royal Academy of Engineering for support. This research was also supported by U.K. EPSRC and the ERC. 'The raw data for this article can be found in the open-access repository at http://dx.doi.org/10.5525/gla.researchdata.364.